Separation of Kondo lattice coherence from crystal electric field in CeIn₃ with Nd substitutions

Jackson R. Badger [1] Rumika Miyawaki,[2] Zach E. Brubaker [3,*] Peter Klavins [3] Rena Zieve,[3]
Tatsuma D. Matsuda,[2] and Valentin Taufour [3]

[1]*Chemistry Department, University of California, Davis, Davis, California 95616, USA*
[2]*Department of Physics, Tokyo Metropolitan University, Hachioji, Tokyo 192-0397, Japan*
[3]*Department of Physics and Astronomy, University of California, Davis, Davis, California 95616, USA*

The $Ce_mM_nIn_{3m+2n}$ ($m = 1, 2$; $n = 0, 1$) family has been one of the most studied families of heavy fermion compounds. This family has revealed many interesting low-temperature physics phenomena, like quantum critical points, heavy fermion superconductivity, and non-Fermi liquid behavior, when these materials are exposed to pressure, magnetic fields, and/or chemical substitution. Here we provide a thorough investigation of the $Ce_{1-x}Nd_xIn_3$ phase diagram through single crystal synthesis, x-ray diffraction, energy-dispersive spectroscopy, magnetic susceptibility, and electrical resistivity measurements. Previous electrical resistivity measurements on CeIn₃ reveal a broad maximum, $T_{max} \sim 50$ K, which has been associated with the Kondo lattice coherence crossover and/or the crystal electric field depopulation effect as the $4f$ electrons condense from the high-energy quartet down to the ground state doublet. Our findings show that in the most disordered substitution region, $x = 0.4$–0.5, these features disjoin to reveal two distinct broad humps in electrical resistivity measurements. Magnetic susceptibility and electrical resistivity data on $Ce_{1-x}Nd_xIn_3$ also reveal the antiferromagnetic ordering competition between CeIn₃ and NdIn₃, where the T_N of CeIn₃ is linearly suppressed to a critical concentration of $x_{Nd} \sim 0.6$. This concentration is slightly lower than what was previously reported in nonmagnetically substituted $Ce_{1-x}La_xIn_3$. Our magnetic susceptibility measurements and subsequent simulations show that in the CeIn₃ antiferromagnetic regime, $x_{Nd} \leqslant 0.4$, the Nd ions act as free paramagnets. The large magnitude of the associated paramagnetic response then masks the overlapping antiferromagnetic ordering signature of the Ce ions. Overall our study further sheds light on the underlying crystal electric field and Kondo lattice coherence interactions within the $Ce_mM_nIn_{3m+2n}$ family and could stimulate further studies of these systems via neutron diffraction or under applied pressure.

I. INTRODUCTION

Explorations of heavy fermion phase diagrams through chemical substitution, hydrostatic pressure, and/or magnetic fields have revealed interesting low-temperature physics like superconductivity, quantum criticality, and non-Fermi liquid behavior [1–5]. Furthermore, the phase diagrams of some Ce-based heavy fermion materials also reveal an interplay between Kondo lattice coherence and crystal electric field (CEF) physics. Unfortunately, both phenomena result from the proximity of the Ce f bands to the Fermi level and therefore make it quite difficult to conclusively discern the origin of one or both features in any particular system.

The $CeMIn_5$ ($M =$ Co, Rh, Ir) family contains many examples of tunable ground states. In these cases the heavy fermion unconventional superconductivity or quantum criticality could result from the different energy scales of the heavy fermionic Kondo lattice coherence and CEF interactions. Inelastic neutron studies have found that these tetragonal materials have two clear and well separate CEF splittings [6]. $\rho_{mag}(T)$ measurements on $CeMIn_5$ samples only show evidence for a single maximum [7–9], although it should be noted that in

anisotropic $\rho(T)$ measurements, there does appear to be limited evidence for at least two separate $-\ln(T)$ regions [10]. Either way the one clear $\rho_{mag}(T)$ maximum observed in these materials has been squarely attributed to the Kondo lattice coherence [11–15].

Within other tetragonal materials with well-separated Kondo lattice coherence and CEF resistivity features, it has been well established that the application of hydrostatic pressure can change the Kondo lattice coherence energy scale (k_BT_{coh}) [16–22]. In many of these cases k_BT_{coh} increases to converge with a CEF depopulation scattering maximum to form a single broad feature. Pressure studies on the $CeMIn_5$ family have also shown that k_BT_{coh} and the associated maximum in $\rho_{mag}(T)$ can shift to higher temperatures [7,10,23,24]. Yet there is no clear evidence that it is possible to separate the Kondo lattice coherence and CEF depopulation features through hydrostatic pressure. Another way to alter k_BT_{coh} in $CeMIn_5$ is by chemical substitution [11–13,25–28]. Within these substituted systems the Kondo coherence maximum for $CeMIn_5$ is driven to lower temperatures with increasing substitution concentrations. Yet again in these systems, there is no evidence that the Kondo lattice coherence and CEF depopulation features separate.

In the base compound of the $CeMIn_5$—CeIn₃—$\rho_{mag}(T)$ experiments also reveal a single broad maximum, $T_{max} \sim$

---
*Present address: Oak Ridge National Laboratory, Oak Ridge, Tennessee 37831, USA.

50 K. However, this feature has been attributed to the combination of the Kondo lattice coherence and the CEF depopulation effects [29–32], wherein the Kondo lattice coherence is only achieved when the $4f$ electrons condense from a high energy Γ_8 quartet to the Γ_7 doublet ground state ($\Delta_{CEF} \sim$ 100–200 K) [33–36]. Similar to CeMIn$_5$, pressure and substitution studies on CeIn$_3$ have shown that this single maximum can be driven to higher [31,37–39] and lower [29,40,41] temperatures, respectively. What remains constant throughout each of these experiments is that only a single resistivity maximum is observed for CeIn$_3$.

Here we report a thorough exploration of Ce$_{1-x}$Nd$_x$In$_3$ to reveal the separation of the Kondo lattice coherence and the CEF depopulation features. Similar to Nd substitutions in CeRhIn$_5$, we argue that the substituted Nd atoms act as Kondo holes and weaken $k_B T_{coh}$ [13]. However, in CeIn$_3$ this results in the Kondo lattice coherence maximum being driven to lower temperatures. This results in two distinct $-\ln(T)$ regions, along with two broad humps, in $\rho_{mag}(T)$, where the low- and high-temperature features stem from the weakened $k_B T_{coh}$ and the persistent CEF energy splitting (Δ_{CEF}), respectively. The Kondo lattice coherence of CeIn$_3$ also seems to follow percolation theory principles because the Nd concentration ($x = 0.65$) that suppresses the Kondo lattice coherence matches the theoretical percolation limit of a simple three-dimensional (3D) cubic system [42]. While a double maximum $\rho_{mag}(T)$ curve has been experimentally observed in other cubic Ce-based materials [43,44], the Kondo lattice coherence and CEF depopulation features have not yet been separated in the well studied Ce$_m$M$_n$In$_{3m+2n}$ ($m = 1, 2$; $n = 0, 1$) family.

Through powder x-ray diffraction (PXRD), energy-dispersive spectroscopy (EDS), magnetization, and electrical resistivity measurements we construct a comprehensive phase diagram, including two antiferromagnetic (AFM) regions. We also discuss the interactions between the two different AFM structures of CeIn$_3$ and NdIn$_3$. Last, in the low concentration region of Nd, $x \leqslant 0.4$, we show how the paramagnetic signal from the Nd^{3+} ions masks the small AFM signature in magnetic susceptibility measurements.

II. MATERIALS AND METHODS

Single-crystalline samples of Ce$_{1-x}$Nd$_x$In$_3$ were grown with a self-flux technique [31,45]. Appropriate atomic percentages (97% In and 3% rare earth) Ce chunks (99.996%, Ames Laboratory), Nd chunks (99.996%, Ames Laboratory), and In shots (99.99%, Alfa Aesar) were placed together in the bottom crucible of a Canfield crucible set [46]. For each synthesis, the alumina crucible set was sealed in an evacuated quartz ampoule and then heated up to and held at 1050 °C for 5 h, after which the reaction was slowly cooled down to 300 °C over a period of 80–100 h to allow for adequate growth of large single crystals. Once at 300 °C the ampoule was then quickly centrifuged to remove the excess In flux. In the end, shiny, silver, blocklike single crystals ranging 1–3 mm were grown in the bottom crucible.

Each synthesis was checked to be single phase by PXRD performed on a Rigaku Miniflex with Cu $K\alpha$ ($\lambda = 1.541\,78$ Å) radiation at room temperature. GSAS-II was used

to perform Pawley refinement on each PXRD pattern to measure the unit-cell parameter for each batch [49]. Si (NIST 640e) was used within each sample as an internal standard. In addition, the elemental composition was measured for selected samples on a Hitachi S-4100T Hitachi HTA America with an Oxford INCA energy dispersive spectrometer.

Resistivity measurements were performed using a low-frequency AC resistance bridge on a Quantum Design physical property measurement system from 300 to 1.8 K. For each measurement, ϕ 25-μm platinum wires were laid in a four-contact configuration with silver epoxy. After the contacts were laid, the epoxy was cured under vacuum at 120 °C in a vacuum oven for 30 min. For some samples, a ^{3}He insert for the PPMS was used for AC resistivity measurements down to 0.4 K. Magnetization measurements were made in a Quantum Design DC magnetic property measurement system. All samples were encased in a plastic straw and measured with an external magnetic field of 1 T.

III. RESULTS AND DISCUSSION

Phase identification for each PXRD pattern is shown in Fig. 1(a). Regardless of the nominal Nd concentration, x_{Nom}, each synthesis produces single crystals that fit to the cubic Cu$_3$Au structure. The PXRD patterns reveal nearly phase pure products with the only other phases consisting of trace amounts of In flux and the internal Si standard. The amount of indium varies for each measurement and depends upon the residual indium stuck on the surface of the selected crystals. Unit-cell parameter a, obtained from Pawley refinements, shows a smooth linear decrease as a function of x_{Nom}, in agreement with Vegard's law [Fig. 1(b)]. This linear relationship indicates that the Nd and Ce atoms homogeneously incorporate into the parent structures at the ends of the substitution range.

Atomic compositions were also obtained from EDS spectra on selected crystals. The substitution percentages obtained from these measurements, x_{EDS}, show good agreement with x_{Nom} [inset of Fig. 1(b)]. However, the two values can differ by up to about 5%, as shown by the dotted lines. Since x_{EDS} and x_{Nom} are in good agreement with one another, henceforth, all values of x_{Nd} will refer to x_{Nom}.

In Fig. 2(a) we present the temperature dependence of the normalized electrical resistivity, $\rho(T)/\rho(300$ K$)$, for single crystals from representative batches of Ce$_{1-x}$Nd$_x$In$_3$. As previously highlighted, the resistivity curve for CeIn$_3$ shows a maximum, $T_{max} \sim 50$ K, which has been associated to the combination of the Kondo lattice coherence and the CEF depopulation effects [29–32]. Tracking T_{max} across the Ce$_{1-x}$Nd$_x$In$_3$ alloys, we find that this feature shifts slightly to lower temperatures with increasing Nd concentration (orange crosses in Fig. 6). This is similar to other substitution studies on CeIn$_3$ [29,32,41,50]. Nd substitution, however, differs because in the most disordered region, $x = 0.4$–0.5, a clear and distinct second maximum arises, T^* shown by the red arrow in Fig. 2(a), and then sharply drops in temperature.

This double maximum behavior can more easily be observed in Fig. 3, where $\rho(T)$ and $M(T)/H$ curves are shown for $x = 0.4$–0.5. Interestingly, we find that the low-temperature maximum (black arrows in Fig. 3) sharply
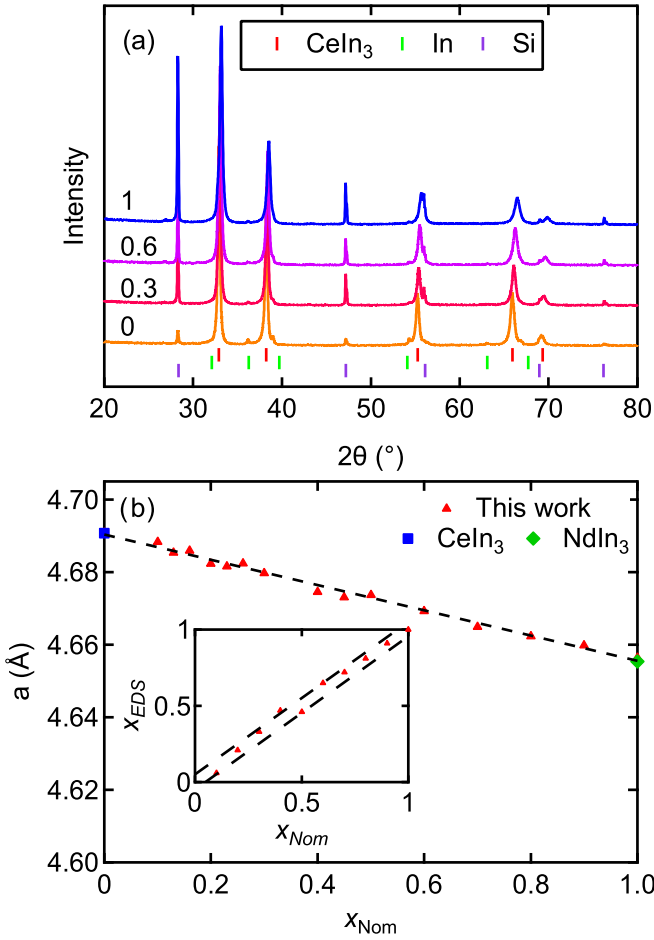
FIG. 1. (a) PXRD patterns for single crystals when $x_{Nom} = 0$, 0.3, 0.6, and 1. (b) Cubic lattice parameter a as a function of x_{Nom} within the $Ce_{1-x}Nd_xIn_3$ series. The unit-cell parameter a for $CeIn_3$ and $NdIn_3$ are from [47] and [48], respectively. The inset shows the relationship between x_{Nom} and x_{EDS}. The two dotted lines are the $\pm 5\%$ error region.

FIG. 2. (a) Normalized temperature dependence of $\rho(T)/\rho(300\ K)$ for representative single crystals of $Ce_{1-x}Nd_xIn_3$. The red arrow shows the low-temperature maximum T_{coh} for $x = 0.4$. The inset shows examples of the peak associated with the AFM transition in the first-derivative curve, $d\rho(T)/dT$, from $CeIn_3$, $Ce_{0.6}Nd_{0.4}In_3$, and $NdIn_3$. The arrows show the midpoint that was selected for T_N^ρ. (b) $\rho_{mag}(T)$ for $CeIn_3$ and $Ce_{0.55}Nd_{0.45}In_3$. The log scale is used to show the regions with a $-\ln(T)$ relationship (dashed black lines) indicating the CEF depopulation and/or the Kondo lattice coherence effects. The inset shows the zoomed-in low-temperature region for $Ce_{0.55}Nd_{0.45}In_3$ where the second maximum, T_{coh}, and $-\ln(T)$ region are more easily observed.

decreases in temperature and seems to approach 0 K near the theoretical percolation threshold for a simple 3D cubic system ($x = 0.65$) (solid black line in Fig. 6) [42].

We note that the low-temperature maximum in resistivity is observed at temperatures lower than the Néel temperature of pure $CeIn_3$ at $T_N = 10.2$ K. Often, an enhancement in resistivity below the magnetic ordering can be observed because of nesting. It is therefore important to consider the possibility that the observed maximum in resistivity is clearly distinguished from the anomaly corresponding to the magnetic ordering. For $x = 0.4$ and $x = 0.45$ the antiferromagnetic orderings are observed in resistivity as a clear kink at 3.44 and 2.56 K, respectively, and we can estimate the width as ± 1.22 K and ± 0.54 K, respectively, as defined by the difference between the mid and maximum points in the first derivative. On the other hand, the low-temperature resistivity maximum occurs at 7.14 K for $x = 0.4$, and 6.00 K for $x = 0.45$. Therefore, we can conclude that, despite their proximity, the magnetic ordering temperature and the low-temperature maximum in resistivity are two distinct temperatures. By contrast, the maximum resistivity in the range $x = 0.6$–0.8
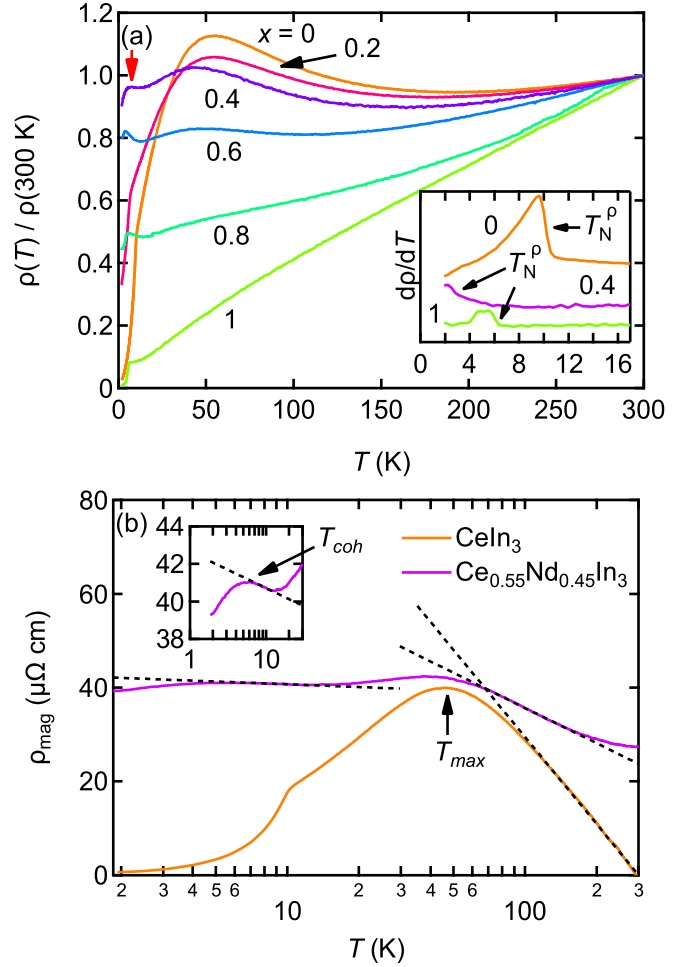
corresponds to a magnetic transition for the Nd ordering, which is shown in Fig. 3 for $x = 0.6$.

Figure 2(b) shows $\rho_{mag}(T)$ for $CeIn_3$ and $Ce_{0.55}Nd_{0.45}In_3$ where the phonon scattering was subtracted out by their respective La analogs: $LaIn_3$ and $La_{0.55}Nd_{0.45}In_3$. By substituting Nd into the $CeIn_3$ structure, the high-temperature $-\ln(T)$ relationship and T_{max} are preserved, while for the most disordered substitution concentrations (e.g., $Ce_{0.55}Nd_{0.45}In_3$) a second maximum, T^*, arises which also contains a temperature region with the $-\ln(T)$ relationship [inset Fig. 2(b)]. These $-\ln(T)$ regions in $\rho_{mag}(T)$ are expected for both features [15,51].

Here we argue that this double maximum occurs due to the separation of the Kondo lattice coherence and CEF
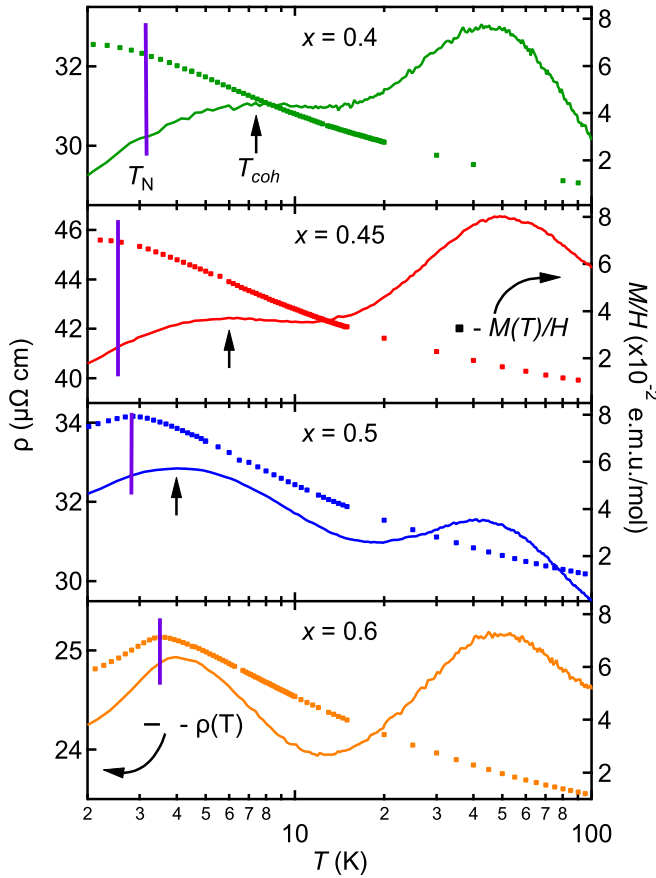
FIG. 3. $\rho(T)$ (lines) and $M(T)/H$ (squares) for $x = 0.4$ (green), 0.45 (red), 0.5 (blue), and 0.6 (orange). The purple vertical lines show the location of the T_N from $\rho(T)$ data and the black arrows shows the location of T_{coh}.
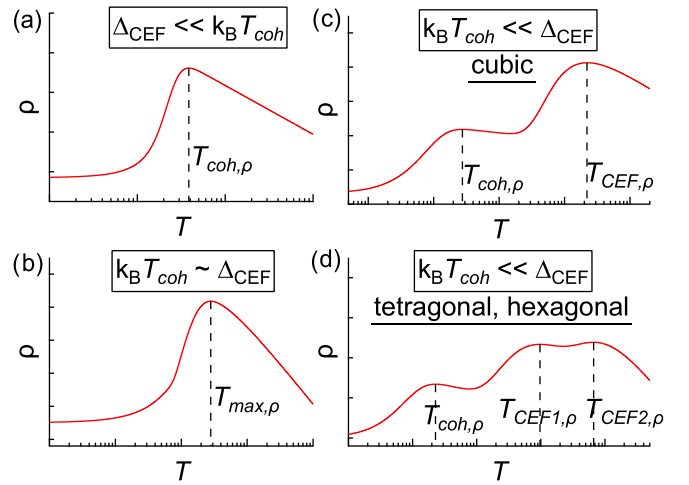

FIG. 4. Schematics of the temperature dependence of the electrical resistivity for a Kondo lattice (ignoring phonon contributions). (a) the CEF splitting energy Δ_{CEF} is smaller than the Kondo coherence energy scale T_{coh}. (b) Δ_{CEF} and $k_B T_{coh}$ are of similar magnitude. (c), (d) $k_B T_{coh}$ is smaller than Δ_{CEF}. In cubic symmetry (c), there are two resistivity maxima associated with the coherence and CEF effects. In hexagonal or tetragonal symmetries (d), there can be a third maxima associated with the additional CEF energy splitting.

depopulation features. More specifically the Nd ions act as Kondo holes and lower T_{coh} [52,53]. The Nd substitution drives the Kondo lattice coherence crossover of CeIn$_3$ to lower temperatures until this feature disjoins from the CeIn$_3$ CEF depopulation feature. Meanwhile the incoherent Kondo scattering from the CEF interaction operates at the local level on the Ce ions, so Δ_{CEF} is not expected to change much with varying the Ce concentration. Therefore, the persistent $T_{max,\rho}$ remains associated with the CEF depopulation effect feature and the second maximum, $T^* = T_{coh}$, at lower temperature is attributed to the weakened Kondo lattice coherence. Overall these data show that the Kondo lattice coherence and the CEF depopulation effects are independent and can be separated by Nd substitutions. In the parent compound CeIn$_3$, the overlap of the two features results from the accidental similarity of the two energy scales. Additionally, since T_{coh} is completely suppressed near the theoretical percolation limit for a simple 3D cubic system it then follows that the Kondo lattice coherence follows percolation theory principles.

In Fig. 4 we show different schematics of $\rho_{mag}(T)$ curves for Ce-based systems, with each schematic representing one of the possible scaling relations between $k_B T_{coh}$ and Δ_{CEF}. Panels (c) and (d) show the difference between a cubic and tetragonal/hexagonal system when $k_B T_{coh} \ll \Delta_{CEF}$, respectively. If a system, like CeIn$_3$, has $\Delta_{CEF} \sim k_B T_{coh}$ then the

$\rho_{mag}(T)$ curve has one maximum [label $T_{max,\rho}$ in Fig. 4(b)]. When $k_B T_{coh} \ll \Delta_{CEF}$ (like in CeAl$_2$ [43] or CeMg$_3$ [44]) then each Δ_{CEF} should be observed as a depopulation maximum and the lowest temperature maximum can be associated with the Kondo lattice coherence [Figs. 4(c) and 4(d)]. These curve shapes could also be achieved by lowering $k_B T_{coh}$ with chemical substitution. But this can only be achieved if the parent compound had $\Delta_{CEF} \sim k_B T_{coh}$. However, if $k_B T_{coh} \gg \Delta_{CEF}$ then only one maximum is expected when the system undergoes a Kondo lattice coherence crossover [Fig. 4(a)]. Given the similarities between the curves of Figs. 4(a) and 4(b) it is not possible to infer the relative nature of $k_B T_{coh}$ and Δ_{CEF} in a Ce-based compound from just a resistivity measurement on the parent compound. However, by performing chemical substitution it is possible to elucidate the relative nature of the two.

We can use tetragonal CeMIn$_5$ as an example. In all compounds among this family only one maximum is observed in $\rho(T)$ [7–9]. Based on our schematics this would then indicate that either $\Delta_{CEF,high} \ll k_B T_{coh}$ or that $\Delta_{CEF,high} \sim k_B T_{coh}$. In the latter situation performing chemical substitution would weaken $k_B T_{coh}$ and eventually give rise to at least one additional well-separated maximum in $\rho_{mag}(T)$. Since this has not been observed in any Ce site chemical substitution study on these tetragonal systems it indicates that the former situation ($\Delta_{CEF,high} \ll k_B T_{coh}$) is the most likely scenario [11–13,25,26,28,54]. Hence, as previously suggested, the single maximum in $\rho_{mag}(T)$ observed in CeMIn$_5$ can be attributed to the Kondo lattice coherence [11–13,15]. It should be noted that this assessment does appear to be in conflict with the large Δ_2 values in these materials [6]. However, $T_{CEF,\rho}$ is the result of the CEF effect on the single impurity Kondo temperature [51,55], so that in many systems $\Delta_{CEF} \neq k_B T_{CEF,\rho}$.

So it is also possible that in CeMIn$_5$ the Kondo exchange lowers $T_{\text{CEF},\rho}$ below $T_{\text{coh},\rho}$.

Ultimately our work shows that it is possible to separate the Kondo lattice coherence and CEF features within the Ce$_m M_n$In$_{3m+2n}$ family. We highlight that a double maximum feature has been observed in previous substitution studies on CeIn$_3$ and our work makes clear the underlying mechanism behind this unique feature [32,40].

It should be noted that previous Kondo holes were strictly associated with nonmagnetic atoms [52,53]. Although it is well established that Nd^{3+} ions produce magnetic materials, from a Kondo/CEF physics perspective these ions act more like their nonmagnetic counterparts, La^{3+}. This is due to the low-lying 4f Nd bands [56] and their inability to induce the Kondo effect with the conduction electrons. Similar arguments have been made about magnetic substitution studies on CeMIn$_5$ [13,27,57,58].

Evidence for the AFM ordering transition is observed as a downward kink in the resistivity [inset Fig. 2(a)] and magnetic susceptibility, $M(T)/H$, curves [inset Fig. 5(a)]. The midpoint of the first-derivative peak, $d\rho/dT$, matches well with the magnetic susceptibility AFM transitions. For the two parent compounds, CeIn$_3$ and NdIn$_3$, the transitions, T_N^ρ and T_N^M, match the T_N^M temperatures from previous reports: $T_N^M = 10.2$ and 5.9 K, respectively [33,35,59,60].

Interestingly, unlike the magnetic data, the $\rho(T)$ data show evidence for a single T_N^ρ in the Nd dilute region, $x_{\text{Nd}} \leqslant 0.4$. This T_N^ρ is then suppressed to lower temperatures as a function of x_{Nd} until the transition temperature is reduced down to ~2.5 K when $x_{\text{Nd}} = 0.45$. Above this concentration of Nd, both resistivity and magnetic susceptibility measurements reveal a clear single AFM transition which increases with x_{Nd}. Samples with low Nd substitution show no obvious AFM transitions in magnetization measurements; rather samples within this region appear to have a large paramagnetic signal at low temperatures. The lone exception is when $x_{\text{Nd}} = 0.1$ there is a small kink around 8.5 K, as denoted by the arrow in Fig. 5(b).

Similar magnetic susceptibility results—lack of AFM transition—were observed when Gd, Tb, and Dy were separately alloyed into CeIn$_3$ at low concentrations [41]. In the Ce-concentrated regions of these materials, however, electrical transport measurements also revealed the continued presence and suppression of the CeIn$_3$ AFM transition. The authors did not directly comment on this discrepancy in the Gd, Tb, and Dy alloys. However, when substituted with nonmagnetic La atoms, clear CeIn$_3$ AFM transitions are observed in magnetic susceptibility measurements with similar Ce concentrations in Ce$_{1-x}$La$_x$In$_3$ [40]. Therefore, to explain the absence of a visible AFM anomaly from our samples, we hypothesize that the large magnetic signal from paramagnetic Nd^{3+} ions dominates the smaller signal associated with the antiferromagnetic ordering of the CeIn$_3$ lattice.

To test this hypothesis we calculated theoretical curves by taking a weighted sum between the antiferromagnetically aligned CeIn$_3$ lattice (with the same T_N) and the paramagnetic Nd ions. These calculations require two key assumptions about these alloys: (1) the Ce moments aligned antiferromagnetically in accordance with the CeIn$_3$ lattice and (2) the Nd moments are too dilute to order magnetically and thus remain paramagnetic throughout the temperature region.

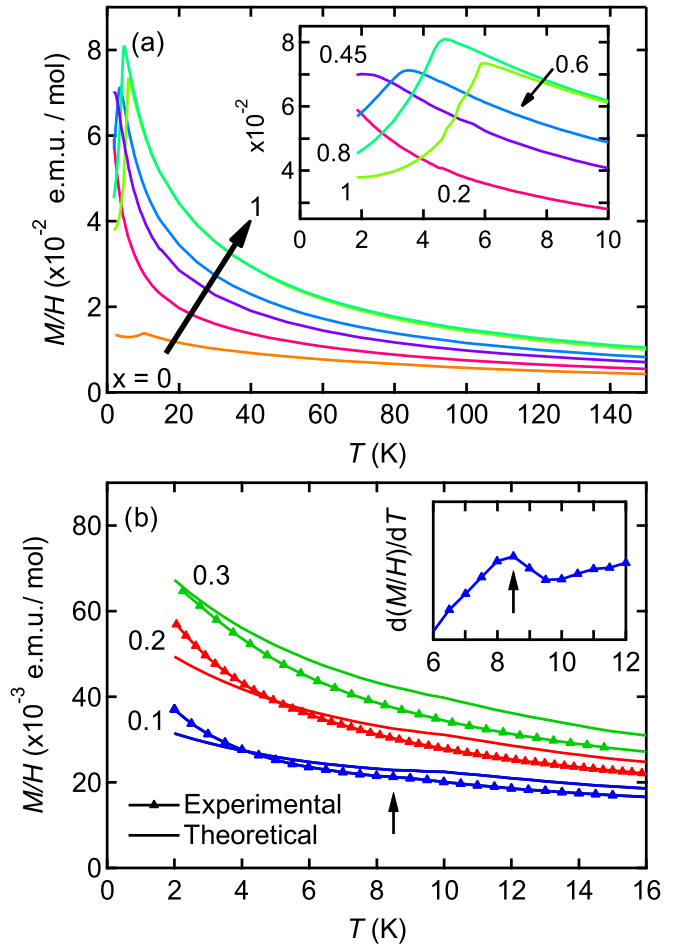FIG. 5. (a) Temperature dependence of $M(T)/H$ from selected samples in the Ce$_{1-x}$Nd$_x$In$_3$ series. These measurements were collected in a $\mu_0 H = 1$ T field. Given the cubic nature of structure, crystal orientation was not accounted for. Inset shows the low-temperature region of the susceptibility curves for $x_{\text{Nd}} = 0.2$–1. (b) The experimental data for $x_{\text{Nd}} = 0.1$, 0.2, and 0.3 are shown by the lines with triangles. The solids lines represent the simulated data for the respective values of x_{Nd}. For these simulations, the calculated μ_{eff} for a Nd^{3+} of $3.62\mu_B$ and a Curie-Weiss constant of $\theta = -6.67$ K were employed to represent the Nd magnetic contributions. The arrow shows the slight kink where the Ce^{3+} AFM transition is experimentally observed from Ce$_{0.9}$Nd$_{0.1}$In$_3$. Inset: the temperature derivative of the $M(T)/H$ curve for $x = 0.1$ which better shows the transition as a maximum.

Using the raw data of CeIn$_3$ and the theoretical μ_{eff} of Nd, a weighted sum was applied across the entire temperature range [Fig. 5(b)]. To get a comparable Curie-Weiss constant for each weighted sum we first performed a least-squares fitting on the $x = 0.1$ curve in the range 20–300 K and obtained $\theta_{\text{CW}} = -6.67$ K. We then used this value for the $x = 0.2$ and 0.3 weighted sums. When $x_{\text{Nd}} = 0.1$, both the simulated and experimental curves show a slight kink in the upward susceptibility curves, originating from the CeIn$_3$ AFM ordering. The simulated curves for $x_{\text{Nd}} = 0.2$ and 0.3 appear in reasonable agreement with the experimental data and show that the CeIn$_3$ AFM transitions are indiscernible. Therefore, across this region, $x_{\text{Nd}} \leqslant 0.4$, we conclude that the Nd ions
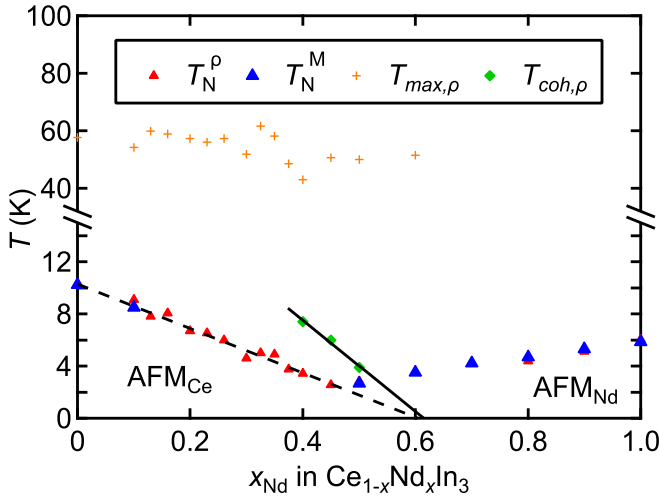
FIG. 6. Observed features from $\rho(T)$ and $M(T)/H$ curves as a function of x_{Nd} for $Ce_{1-x}Nd_xIn_3$. The two AFM regions, AFM_{Ce} and AFM_{Nd}, show the Nd concentrations where the $CeIn_3$ and $NdIn_3$ AFM structures, respectively, are dominant. The dotted black line is the linear fit of T_N^ρ and T_N^M for the $CeIn_3$ region when $x_{Nd} \leqslant 0.4$. The solid black line is the linear fit of the second maximum, T_{coh}, for $x = 0.4, 0.45$, and 0.5.

do not participate in the magnetic ordering of $CeIn_3$ and remain paramagnetic, leading to the larger Nd paramagnetic signal masking the magnetic signature from the $CeIn_3$ AFM ordering.

The AFM transitions from the magnetic susceptibility and electrical transport measurements are combined with the resistivity features discussed above to create a comprehensive $T - x_{Nd}$ phase diagram (Fig. 6). Instead of adopting the other's AFM structure, the $CeIn_3$ and $NdIn_3$ AFM orderings appear to be in competition with one another and each weakens the magnetic ordering of the other lattice. Similar to the La substituted system, there is a linear dependence of T_N with x_{Nd} in the Ce-concentrated region which extrapolates to give a critical concentration of $x_c \sim 0.6$ (dotted black line Fig. 6) [26]. Like the critical concentration for the Kondo lattice coherence, x_c is in good agreement for the percolation threshold, $x = 0.65$, for a simple cubic lattice [42]. However, the slight drop from $x_c = 0.65$ to 0.6 indicates that there could be an additional mechanism at play like magnetic frustration

due to the different AFM structures of $CeIn_3$ and $NdIn_3$. This behavior was observed in the Nd-substituted $CeRhIn_5$ system [13].

IV. CONCLUSIONS

We have shown that Nd can successfully substitute into the parent $CeIn_3$ compound via a self-flux technique with excess In. Our PXRD and EDS results reveal a direct relationship between the nominal and actual substitution concentrations as Nd homogenously incorporates into the structure until it becomes fully $NdIn_3$. Our electrical resistivity measurements reveal that as Nd incorporates into the $CeIn_3$ structure, the Kondo lattice coherence and CEF depopulation features disjoin to reveal double maximum curves with two distinct $-\ln(T)$ regions. We argue that the high-temperature maximum results from CEF depopulation effect from the splitting Δ_{CEF} in $CeIn_3$ and in the most disordered region ($x = 0.4$–0.5) the Nd ions act as Kondo holes to weaken $k_B T_{coh}$ and push the Kondo lattice coherence crossover to lower temperatures. It appears that the Kondo lattice coherence feature disappears near the theoretical percolation limit for a simple 3D cubic system, which suggests that this Kondo lattice coherence abides by percolation theory principles. The Kondo lattice coherence and CEF depopulation phenomena are shown to separate for a material within the $Ce_mM_nIn_{3m+2n}$ ($m = 1, 2; n = 0, 1$) family. Magnetic and resistivity measurements also reveal that across the substitution values, there is an interesting competition between the magnetic orderings of the two parent structures $CeIn_3$ and $NdIn_3$. Rather than adopting the AFM structure of the end parent structures, Ce and Nd ions act as free paramagnets, when in dilute concentrations. The comprehensive phase diagram reveals a $x_c \sim 0.6$ which is slightly lower than observed for nonmagnetically substituted $CeIn_3$. Future neutron diffraction and pressure studies on $Ce_{1-x}Nd_xIn_3$ would be valuable to further understand the interplay between these two AFM orders.

[1] P. Gegenwart, Q. Si, and F. Steglich, Nat. Phys. **4**, 186 (2008).

[2] T. Park, Y. Tokiwa, F. Ronning, H. Lee, E. D. Bauer, R. Movshovich, and J. D. Thompson, Phys. Status Solidi B **247**, 553 (2010).

[3] P. J. W. Moll, T. Helm, S.-S. Zhang, C. D. Batista, N. Harrison, R. D. McDonald, L. E. Winter, B. J. Ramshaw, M. K. Chan, F. F. Balakirev, B. Batlogg, E. D. Bauer, and F. Ronning, npj Quantum Mater. **2**, 46 (2017).

[4] D. Aoki, K. Ishida, and J. Flouquet, J. Phys. Soc. Jpn. **88**, 022001 (2019).

[5] S. Ran, C. Eckberg, Q.-P. Ding, Y. Furukawa, T. Metz, S. R. Saha, I.-L. Liu, M. Zic, H. Kim, J. Paglione, and N. P. Butch, Science **365**, 684 (2019).

[6] A. D. Christianson, E. D. Bauer, J. M. Lawrence, P. S. Riseborough, N. O. Moreno, P. G. Pagliuso, J. L. Sarrao, J. D. Thompson, E. A. Goremychkin, F. R. Trouw, M. P. Hehlen, and R. J. McQueeney, Phys. Rev. B **70**, 134505 (2004).

[7] H. Hegger, C. Petrovic, E. G. Moshopoulou, M. F. Hundley, J. L. Sarrao, Z. Fisk, and J. D. Thompson, Phys. Rev. Lett. **84**, 4986 (2000).

[8] C. Petrovic, P. G. Pagliuso, M. F. Hundley, R. Movshovich, J. L. Sarrao, J. D. Thompson, Z. Fisk, and P. Monthoux, J. Phys.: Condens. Matter **13**, L337 (2001).

[9] C. Petrovic, R. Movshovich, M. Jaime, P. G. Pagliuso, M. F. Hundley, J. L. Sarrao, Z. Fisk, and J. D. Thompson, Europhys. Lett. **53**, 354 (2001).

[10] Z. Ren, G. W. Scheerer, D. Aoki, K. Miyake, S. Watanabe, and D. Jaccard, Phys. Rev. B **96**, 184524 (2017).

[11] C. Petrovic, S. L. Bud'ko, V. G. Kogan, and P. C. Canfield, Phys. Rev. B **66**, 054534 (2002).

[12] J. Paglione, T. A. Sayles, P.-C. Ho, J. R. Jeffries, and M. B. Maple, Nat. Phys. **3**, 703 (2007).

[13] P. F. S. Rosa, A. Oostra, J. D. Thompson, P. G. Pagliuso, and Z. Fisk, Phys. Rev. B **94**, 045101 (2016).

[14] Y.-f. Yang, D. Pines, and G. Lonzarich, Proc. Natl. Acad. Sci. USA **114**, 6250 (2017).

[15] S. Jang, J. D. Denlinger, J. W. Allen, V. S. Zapf, M. B. Maple, J. N. Kim, B. G. Jang, and J. H. Shim, Proc. Natl. Acad. Sci. USA **117**, 23467 (2020).

[16] D. Jaccard, K. Behnia, and J. Sierro, Phys. Lett. A **163**, 475 (1992).

[17] D. Jaccard, H. Wilhelm, K. Alami-Yadri, and E. Vargoz, Phys. B (Amsterdam, Neth.) **259-261**, 1 (1999).

[18] E. Vargoz and D. Jaccard, J. Magn. Magn. Mater. **177–181**, 294 (1998).

[19] A. T. Holmes, D. Jaccard, and K. Miyake, Phys. Rev. B **69**, 024508 (2004).

[20] Y. Kawamura, T. Nishioka, H. Kato, M. Matsumura, K. Matsubayashi, and Y. Uwatoko, J. Phys.: Conf. Ser. **200**, 012082 (2010).

[21] Z. Ren, L. V. Pourovskii, G. Giriat, G. Lapertot, A. Georges, and D. Jaccard, Phys. Rev. X **4**, 031055 (2014).

[22] Y. Hayashi, S. Takai, T. Matsumura, H. Tanida, M. Sera, K. Matsubayashi, Y. Uwatoko, and A. Ochiai, J. Phys. Soc. Jpn. **85**, 034704 (2016).

[23] M. Nicklas, R. Borth, E. Lengyel, P. G. Pagliuso, J. L. Sarrao, V. A. Sidorov, G. Sparn, F. Steglich, and J. D. Thompson, J. Phys.: Condens. Matter **13**, L905 (2001).

[24] Y. Takaesu, N. Aso, Y. Tamaki, M. Hedo, T. Nakama, K. Uchima, Y. Ishikawa, K. Deguchi, and N. K. Sato, J. Phys.: Conf. Ser. **273**, 012058 (2011).

[25] S. Nakatsuji, S. Yeo, L. Balicas, Z. Fisk, P. Schlottmann, P. G. Pagliuso, N. O. Moreno, J. L. Sarrao, and J. D. Thompson, Phys. Rev. Lett. **89**, 106402 (2002).

[26] P. G. Pagliuso, N. O. Moreno, N. J. Curro, J. D. Thompson, M. F. Hundley, J. L. Sarrao, Z. Fisk, A. D. Christianson, A. H. Lacerda, B. E. Light, and A. L. Cornelius, Phys. Rev. B **66**, 054433 (2002).

[27] Y. P. Singh, D. J. Haney, I. K. Lum, B. D. White, M. B. Maple, M. Dzero, and C. C. Almasan, J. Phys.: Conf. Ser. **592**, 012078 (2015).

[28] N. Pouse, S. Jang, B. D. White, S. Ran, R. B. Adhikari, C. C. Almasan, and M. B. Maple, Phys. Rev. B **97**, 235149 (2018).

[29] R. Elenbaas, C. Schinkel, and C. van Deudekom, J. Magn. Magn. Mater. **15–18**, 979 (1980).

[30] M. Lavagna, C. Lacroix, and M. Cyrot, J. Phys. F **12**, 745 (1982).

[31] G. Knebel, D. Braithwaite, P. C. Canfield, G. Lapertot, and J. Flouquet, Phys. Rev. B **65**, 024425 (2001).

[32] N. Berry, E. M. Bittar, C. Capan, P. G. Pagliuso, and Z. Fisk, Phys. Rev. B **81**, 174413 (2010).

[33] A. V. Diepen, R. Craig, and W. Wallage, J. Phys. Chem. Solids **32**, 1867 (1971).

[34] J. M. Lawrence and S. M. Shapiro, Phys. Rev. B **22**, 4379 (1980).

[35] A. Benoit, J. Boucherle, P. Convert, J. Flouquet, J. Palleau, and J. Schweizer, Solid State Commun. **34**, 293 (1980).

[36] W. Knafo, S. Raymond, B. Fåk, G. Lapertot, P. C. Canfield, and J. Flouquet, J. Phys.: Condens. Matter **15**, 3741 (2003).

[37] P. Morin, C. Vettier, J. Flouquet, M. Konczykowski, Y. Lassailly, J. M. Mignot, and U. Welp, J. Low Temp. Phys. **70**, 377 (1988).

[38] T. Kagayama and G. Oomi, Jpn. J. Appl. Phys. **32**, 318 (1993).

[39] F. M. Grosche, I. R. Walker, S. R. Julian, N. D. Mathur, D. M. Freye, M. J. Steiner, and G. G. Lonzarich, J. Phys.: Condens. Matter **13**, 2845 (2001).

[40] Y. Iwamoto, T. Ebihara, N. Harrison, M. Jaime, A. Silhanek, K. Tezuka, K. Morishita, T. Terashima, and A. Iyo, J. Magn. Magn. Mater. **310**, 300 (2007).

[41] M. B. T. Tchokonté, K. G. Tshabalala, P. de Villiers du Plessis, and D. Kaczorowski, J. Phys. Chem. Solids **71**, 181 (2010).

[42] D. Stauffer and A. Aharony, *Introduction to Percolation Theory*, 2nd ed. (Taylor & Francis, London,1992).

[43] Y. Ōnuki, Y. Furukawa, and T. Komatsubara, J. Phys. Soc. Jpn. **53**, 2734 (1984).

[44] P. K. Das, N. Kumar, R. Kulkarni, and A. Thamizhavel, Phys. Rev. B **83**, 134416 (2011).

[45] P. C. Canfield and Z. Fisk, Philos. Mag. B **65**, 1117 (1992).

[46] P. C. Canfield, T. Kong, U. S. Kaluarachchi, and N. H. Jo, Philos. Mag. **96**, 84 (2016).

[47] E. G. Moshopoulou, R. M. Ibberson, J. L. Sarrao, J. D. Thompson, and Z. Fisk, Acta Cryst. B **62**, 173 (2006).

[48] I. Harris and G. Raynor, J. Less-Common Met. **9**, 7 (1965).

[49] B. H. Toby and R. B. Von Dreele, J. Appl. Cryst. **46**, 544 (2013).

[50] P. Pedrazzini, M. Gómez Berisso, N. Caroca-Canales, M. Deppe, C. Geibel, and J. G. Sereni, Eur. Phys. J. B **38**, 445 (2004).

[51] B. Cornut and B. Coqblin, Phys. Rev. B **5**, 4541 (1972).

[52] E. D. Bauer, Y.-F. Yang, C. Capan, R. R. Urbano, C. F. Miclea, H. Sakai, F. Ronning, M. J. Graf, A. V. Balatsky, R. Movshovich, A. D. Bianchi, A. P. Reyes, P. L. Kuhns, J. D. Thompson, and Z. Fisk, Proc. Natl. Acad. Sci. USA **108**, 6857 (2011).

[53] J. D. Thompson, Proc. Natl. Acad. Sci. USA **108**, 18191 (2011).

[54] R. Hu, Y. Lee, J. Hudis, V. F. Mitrovic, and C. Petrovic, Phys. Rev. B **77**, 165129 (2008).

[55] V. Taufour, H. Hodovanets, S. K. Kim, S. L. Bud'ko, and P. C. Canfield, Phys. Rev. B **88**, 195114 (2013).

[56] Y. Kubo, S. Asano, H. Harima, and A. Yanase, Physica B **186–188**, 132 (1993).

[57] C. Capan, G. Seyfarth, D. Hurt, A. D. Bianchi, and Z. Fisk, J. Phys.: Conf. Ser. **273**, 012027 (2011).

[58] M. Shimozawa, T. Watashige, S. Yasumoto, Y. Mizukami, M. Nakamura, H. Shishido, S. K. Goh, T. Terashima, T. Shibauchi, and Y. Matsuda, Phys. Rev. B **86**, 144526 (2012).

[59] A. Czopnik, N. Iliew, B. Staliński, C. Bazan, H. Mädge, and R. Pott, Physica B+C **130**, 259 (1985).

[60] M. Amara, R. Galéra, P. Morin, J. Voiron, and P. Burlet, J. Magn. Magn. Mater. **131**, 402 (1994).